Journal of Materials Chemistry A

Accepted Manuscript

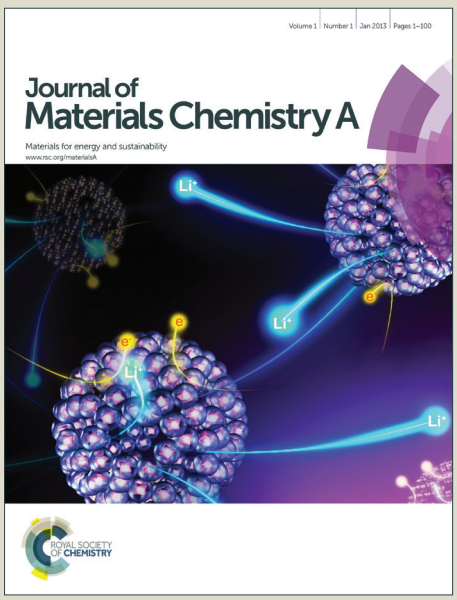

ROYAL SOCIETY OF CHEMISTRY

www.rsc.org/materialsA

Journal Name RSCPublishing

ARTICLE

Fe_3O_4/reduced graphene oxide with enhanced electrochemical performances towards lithium storage

Cite this: DOI: 10.1039/x0xx00000x

Received 00th January 2012,
Accepted 00th January 2012

DOI: 10.1039/x0xx00000x

www.rsc.org/

Chaolun Liang,[ab] Teng Zhai,[a] Wang Wang,[a] Jian Chen,[b] Wenxia Zhao,[b] Xihong Lu*[a] and Yexiang Tong,*[a]

In this work, we reported the facile synthesis of the Fe_3O_4/reduced-graphene oxide (RGO) nanocomposites and their improved lithium storage capability. Fe_3O_4/RGO composites synthesized by a facile co-precipitate method exhibited outstanding electrochemical performance with good cycling stability. As an anode material for Lithium ion batteries (LIBs), the Fe_3O_4/RGO composites achieved a high reversible capacity of 1637 mA h g^{-1} (0.1 A g^{-1}) at the 10th cycle and still remained 1397 mA h g^{-1} after 100 cycles. Moreover, the Fe_3O_4/RGO composites have excellent rate capability. Characterization results reveal that such large reversible capacity is attributed to the synergistic effect between Fe_3O_4 and RGO, which the Fe_3O_4 nanoparticles (NPs) with surface step atoms offer abundant electrochemical active sites for lithium storage and RGO acts as a volume buffer and electron conductor, and more importantly preserves the electrochemical active surfaces and avoids the aggregation of the Fe_3O_4 NPs.

Introduction

Nowadays, with the increasing demand of electric vehicle and portable electric equipment, rechargeable lithium ion batteries (LIBs) with high energy density, high power density, high rate capability and long-term stability are urgently required.[1-5] In the past decade, transition metal oxides have been intensively investigated as anodes in LIBs because they have higher theoretical specific capacities (500~1000 mA h g^{-1}) than the graphite (372 mA h g^{-1}).[6,7] Among various available transition metal oxide anodes, Fe_3O_4 with the theoretical capacities of 924 mA h g^{-1}, has been considered as a promising candidate because of its nature abundance, inexpensive, and nontoxic.[8-11] Recent reports have shown that Fe_3O_4 nanoparticles (NPs) exhibited much improved electrochemical performances than their bulk counterparts.[12,13] However, the severe volume expansions (> 200%) and agglomeration of Fe_3O_4 NPs lead to serious capacity loss and poor cycling stability, which greatly hinder its practical application in LIBs.[14]

Combining Fe_3O_4 NPs with carbon materials to form composites represents an effective strategy to overcome these drawbacks, because carbon materials can act as not only a volume buffer but also a barrier to suppress the aggregation of the active NPs during the charging/discharging process.[15,16] Over the past few years, the integration of Fe_3O_4 NPs with carbon materials such as carbon nanotubes[17], activated carbon[18], graphene[19], carbon nanofibers[20], etc. have been adopted to enhance the electrochemical performance of Fe_3O_4. In particular, graphene is widely regarded as a promising matrix to host Fe_3O_4 for its advantages of outstanding electron transport property, large surface area, superior mechanical strength and chemical stability,[21] which can provide a large electrode/electrolyte contact area, a short transport distance and fast diffusion rates for both lithium ions and electrons.[15,22,23] For example, Lian *et al.* developed Fe_3O_4/graphene nanocomposites by a gas/liquid interface reaction, and these composites exhibited a specific capacity of 1048 mA h g^{-1} up to 90 cycles.[24] Ji *et al.* reported a kind of Fe_3O_4/reduced graphene oxide (RGO) composites with a high reversible capacity of more than 900 mA h g^{-1} at 0.05C.[25] Similarly, Su *et al.* fabricated Fe_3O_4/graphene composites by homogeneously distributed Fe_3O_4 NPs with a size of 7 nm onto the surface of graphene and found that they achieved a high reversible specific capacity of 1102 mA h g^{-1} at 100 mA g^{-1}.[26] Despite these progresses, the design and synthesis of high-performance Fe_3O_4/graphene composites anodes are still desirable. On the other hand, little attention has paid to the influence of the surface microstructure of Fe_3O_4 NPs on this kind of composites, although which is of great importance to their electrochemical properties.

In this work, we focused on the development of high-performane Fe_3O_4/RGO composites for LIBs and investigation of the correlation between the detailed microstructure of the Fe_3O_4/RGO composites and their electrochemical performances. Fe_3O_4/RGO composites prepared by a coprecipitation method achieved a high reversible capacity of 1637 mA h g^{-1} (0.1 A g^{-1}) at the 10th cycle and remained 1397 mA h g^{-1} after 100 cycles, which are substantially higher than the reported values.[27-30]

Characterization results reveal that such large reversible capacity is attributed to the nano-sized Fe_3O_4 particles with surface step atoms which offering abundant electrochemical active sites for lithium storage. Moreover, more than acting as a volume buffer and electron conductor, RGO could also preserve the electrochemical active surfaces and avoid the aggregation of the Fe_3O_4 NPs, and thus resulting in readily reaction between active material and electrolyte.

Experimental

Synthesis of Fe_3O_4/RGO nanocomposites

All reagents used were of analytical grade and were used directly without any purification. GO powders were synthesized by a modified Hummers method[31-33] and RGO powders were obtained by reducing these GO powders in the N_2H_4 atmosphere at 85 °C for 12 h. The Fe_3O_4/RGO nanocomposites were prepared by a chemical precipitation process. For a typical synthesis, 200 ml distilled water dispersion containing 0.1 g graphene sheet was homogeneously mixed with 0.08 g $FeCl_2 \cdot 4H_2O$ and 0.2 g $FeCl_3 \cdot 6H_2O$ (Tianjin Shentai Chemical Reagent Co., Ltd.). The reaction mixture was heated at 50 ℃ under a N_2 atmosphere. After the solution was sonicated for 10 min, 10 ml of 8 M NH_4OH aqueous solution was added dropwise to precipitate ferric and ferrous salts. The reaction was carried out at 50 ℃ for 30 min under vigorous magnetic stirring. The Fe_3O_4/RGO product was obtained by magnetic separation and washed with distilled water and ethanol and finally dried under vacuum at 80 ℃. For comparison, bare Fe_3O_4 NPs was prepared by the same chemical precipitation process without the presence of the RGO. The Fe_3O_4/RGO composites with a higher mass loading of 0.81 mg cm^{-2} were also synthesized by triple the mass of $FeCl_2 \cdot 4H_2O$ and $FeCl_3 \cdot 6H_2O$ without changing other conditions.

Electrochemical Measurements

Active materials (Fe_3O_4/RGO, bare Fe_3O_4, RGO), acetylene black (as conductive agent), and polyvinylidene fluoride (PVDF as binder) in a weight ratio of 80:10:10 were dissolved in N-methylpyrrolidone (NMP) to form slurry. Then the slurry was coated onto a copper foil and treated in a vacuum oven at 100 ℃ for 12 h. The electrodes were pressed and cut into disks as anode. Coin cells (CR2032) were fabricated with as synthesized anode, lithium metal as counter electrode, Celgard 2400 as separator, and $LiPF_6$ (1 M) in ethylene carbonate / dimethyl carbonate / diethyl carbonate (EC/DMC/DEC, 1:1:1 vol%) as the electrolyte. The cell was assembled in an Ar-filled glove box. The rate capability and cycle life of the cells were tested in a potential window of 0.01~3 V (vs Li^+/Li) by a battery testing system (LAND CT 2001A). All of the specific capacities were calculated on the basis of the total weight of Fe_3O_4/RGO (0.37 mg cm^{-2}), Fe_3O_4/RGO-2 (0.81 mg cm^{-2}), bare Fe_3O_4 (0.40 mg cm^{-2}), RGO (0.31 mg cm^{-2}).

Material Characterization

The morphology, microstructure, and compositions of the products were characterized by field-emission scanning electron microscopy (FE-SEM, JSM-6330F), X-ray diffractometry (XRD, D8 ADVANCE), transmission electron microscopy (TEM, JEM2010-HR, FEI Tecnai G^2 F30), laser Micro-Raman Spectrometry (Renishaw inVia), photoelectron Spectroscopy (XPS, ESCALab250).

Results and discussion

Fig. 1a shows the typical XRD patterns of the bare Fe_3O_4 NPs and Fe_3O_4/RGO composites. All the diffraction peaks in both bare Fe_3O_4 and Fe_3O_4/RGO samples can be well indexed to the face-centered cubic (fcc) magnetite (JCPDS No.65-3107). The broadened XRD peaks indicate that the size of the Fe_3O_4 NPs was very small. According to the Scherrer equation, the average size of Fe_3O_4 NPs is calculated to be 9.8 nm for bare Fe_3O_4 and 8.3 nm for Fe_3O_4/RGO composites. Raman spectra of the bare Fe_3O_4 and Fe_3O_4/RGO composites were collected t in Fig. 1b. The characteristic Raman scattering peaks at 490 and 670 cm^{-1}, corresponding to the T_{2g} and A_{1g} vibration modes of Fe_3O_4, were observed for both Fe_3O_4 and the Fe_3O_4/RGO composites.[34,35] The peaks at around 1336 and 1600 cm^{-1} are assigned to the D and G-band from graphene, respectively. To further investigate the composition and surface oxidation state of the as-prepared composites, X-ray photoelectron spectroscopy (XPS) analyses were also performed to The XPS survey spectrum of the Fe_3O_4/RGO composites is shown in Fig. S1. Beside C, O and Fe signals, no any signals of impurity are detected, revealing that the product is highly pure. In the spectrum of Fe 2p (Fig. S1b), the peaks of Fe 2p3/2 and Fe 2p1/2 located at 711.12 and 724.65 eV correspond to the magnetite phase. In addition, the satellite peak at about 719.0 eV does not appear, indicating the formation of the Fe_3O_4 instead of Fe_2O_3 in the RGO matrix.[36-38] For carbon, the C1s XPS spectrum in Fig. S1c shows the low-oxygenated C at 284.8 eV, which reveals the efficient reduction of GO.[9,39]

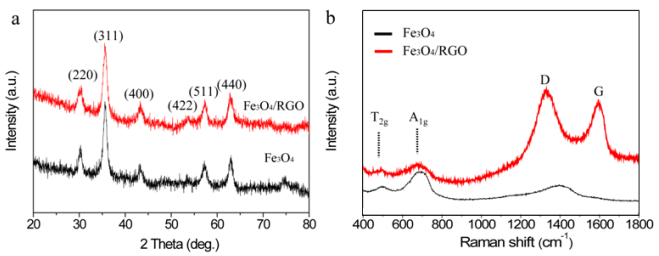

Fig. 1 (a) XRD patterns and (b) Raman spectra collected for bare Fe_3O_4 NPs and Fe_3O_4/RGO composites.

Scanning electron microscopy (SEM) and transmission electron microscopy (TEM) analyses were carried out to study the morphology and detailed microstructure of the Fe_3O_4/RGO composites. SEM image reveals that a lot of Fe_3O_4 NPs are densely and uniformly deposited on RGO surface (Fig. 2a). Fig. 2b displays a typical TEM image of the Fe_3O_4/RGO composites. It is clearly seen that Fe_3O_4 NPs with an average diameter of about 9-11 nm are homogeneously dispersed on the surface of RGO sheets, which is in accordance with SEM result. From the inset of Fig. 2b, the diffraction rings can be indexed to 220, 113 and 400 diffractions of fcc magnetite structure. The bright diffraction rings indicate that the Fe_3O_4 NPs were well crystallized. Fig. 2c illustrates a high resolution TEM (HRTEM) image, showing the microstructure of RGO and Fe_3O_4 NPs. The measured lattice fringes of 0.29 nm and 0.25 nm correspond to the interplanar distances of {220} and {113} plane of magnetite, respectively. Additionally, a characteristic inter-graphene spacing of 0.34 nm was also observed. As shown in Fig. 2d, small particles are easily visible when imaged in scanning TEM (STEM) mode with high-angle annular dark field (HAADF) detector. Moreover, the distributions of Fe, O and C are clearly presented by the STEM-EDS elemental maps (Fig. 2e, f and g),

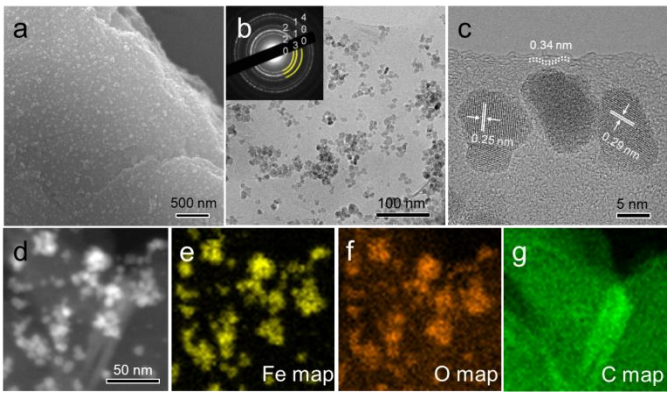

Fig. 2 (a) SEM and (b) TEM bright field image of Fe_3O_4/RGO composites. Inset in (b) shows the corresponding SAED pattern of Fe_3O_4/RGO composites. (c) HRTEM image and (d) HAADF-STEM image of Fe_3O_4/RGO composites. (e-g) STEM-EDS elemental mapping of iron, oxygen, and carbon, respectively.

which indicate that the Fe_3O_4 NPs are uniformly embedded on the RGO matrix. It is worth noting that the Fe_3O_4 NPs are still strongly attached on the surface of RGO sheets even after ultrasonic treatment during the TEM sample preparation process, implying the strong interaction between Fe_3O_4 NPs and RGO sheets.

The electrochemical performances of the Fe_3O_4/RGO composites were investigated using galvanostatic charge-discharge measurements. Fig. 3a presents the charge–discharge voltage profiles of the Fe_3O_4/RGO anode for 1st, 2nd, 10th, 50th, 100th at a current density of 0.1 A g^{-1} between 0.001 and 3.00 V. It can be seen that the Fe_3O_4/RGO composites yielded a very high lithium storage capacity of 3536.8 mA h g^{-1} at the first discharge process, and obtained a reversible capacity of 2189.6 mA h g^{-1} with an initial coulombic efficiency of 61.9%. The irreversible capacity loss is attributed to the inevitable formation of solid electrolyte interphase (SEI) and/or decomposition of electrolytes.[26,40,41] The discharge voltage plateau at around 0.8 V in the first cycle, which is different from other cycles, again confirming the occurred irreversible reactions in the first cycle. The discharge capacities of the Fe_3O_4/RGO anode at 2nd, 10th, 50th, 100th cycles are 2533.1, 1637.1, 1429.3, 1397.3 mA h g^{-1}, respectively. By contrast, the bare Fe_3O_4 anode at 2nd, 10th, 50th, 100th cycles are 625, 200, 75, 75 mA h g^{-1}, respectively. Moreover, the presented capacities of the Fe_3O_4/RGO anode are also substantially higher than hollow-Fe_3O_4/graphene anode (about 1250 mA h g^{-1} at 0.1 A g^{-1}),[27] Fe_3O_4 nanoparticle clusters anode (about 850 mA h g^{-1} at 0.1 A g^{-1}),[28] nitrogen-doped Fe_3O_4/graphene anode (about 1000 mA h g^{-1} at 0.1 A g^{-1}),[29] and Fe_3O_4-CNT composites (about

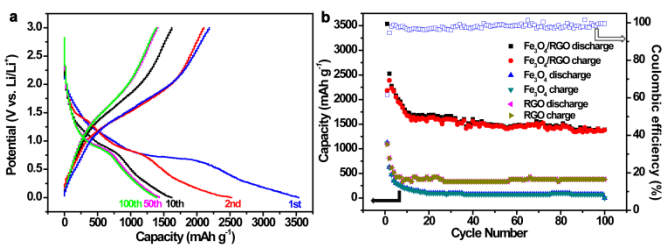

Fig. 3 (a) Charge–discharge voltage profiles of Fe_3O_4/RGO anode at a current density of 0.1 A g^{-1}. (b) Cycling performances of Fe_3O_4/RGO, bare Fe_3O_4, and RGO anode charged and discharged at a current of 0.1 A g^{-1} up to 100 cycles.

1400 mA h g^{-1} at 0.09 A g^{-1}).[30] In addition, the capacity of Fe_3O_4/RGO composites has no obvious change after 50 cycles, indicating its excellent cycling stability. Fig. 3b compares the cycling performances of bare Fe_3O_4, RGO and Fe_3O_4/RGO electrodes at a current of 0.1 A g^{-1} during 100 cycles. Significantly, the Fe_3O_4/RGO electrode exhibited a much higher cycling capacity than the bare Fe_3O_4 and RGO electrodes. For example, the Fe_3O_4/RGO electrode reached a high reversible capacity of 1600 mA h g^{-1} after 10 cycles while only 197 mA h g^{-1} for bare Fe_3O_4 electrode and 393 mA h g^{-1} for RGO electrode. After 100 cycles, the Fe_3O_4/RGO electrode still retained 1397.3 mA h g^{-1} while the bare Fe_3O_4 and RGO electrodes maintained about 75 and 381 mA h g^{-1}. On the other hand, the coulombic efficiency of the Fe_3O_4/RGO electrode is almost 100% during the 100 cycles, suggesting the facile lithium insertion/extraction associated with efficient transport of ions and electrons within the electrodes.[42] The enhanced electrochemical performance of Fe_3O_4/RGO composites can be attributed to the synergistic effect between RGO and Fe_3O_4 and the enhanced conductivity of Fe_3O_4/RGO electrode.

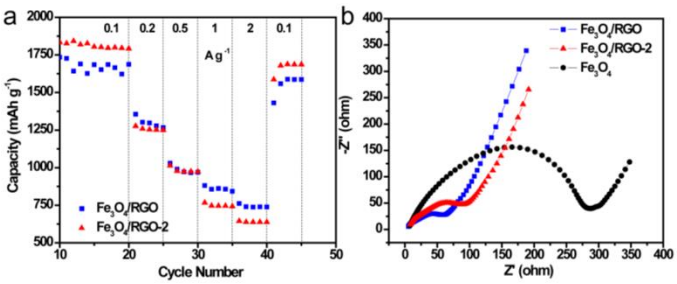

Fig. 4 (a) Rate capability of the Fe_3O_4/RGO and Fe_3O_4/RGO-2 electrodes at different current densitiesfor 45 cycles. (b) Nyquist plots of Fe_3O_4/RGO, Fe_3O_4/RGO-2 and bare Fe_3O_4 electrodes at fresh coin cells over the frequency range from 100 kHz to 0.01 Hz.

Rate performance is a key factor for successful practical application as anode electrode. The Fe_3O_4/RGO composites also possessed a high rate capability. As shown in Fig. 4a, the Fe_3O_4/RGO composites achieved very high capacities of 1637, 1266, 965, 839, 721 mA h g^{-1} at 0.1, 0.2, 0.5, 1 and 2 A g^{-1}, respectively. These values are much higher than those of the bare Fe_3O_4 NPs (Fig. S2). Moreover, a capacity of 1588 mA h g^{-1} was still recoverable (only 3% loss of initial capacity) when the current rate was returned to 0.1 A g^{-1}. The excellent rate capability of Fe_3O_4/RGO composites is considerably higher and comparable to the reported values for other Fe_3O_4/carbon materials composites, such as hollow-Fe_3O_4/grahpene sheet anode (about 40% from 0.1~2 A g^{-1}),[27] nitrogen-doped Fe_3O_4/graphene anode (about 61.6% from 0.1~1.6 A g^{-1}),[29] and Fe_3O_4-CNT composites (about 48.2% from 0.09~1.8 A g^{-1}).[30] Additionally, we have also studied the effect of the mass loading of Fe_3O_4 on the rate capability of the Fe_3O_4/RGO composites. Fe_3O_4/RGO composite with a high Fe_3O_4 mass loading of 0.81 mg cm^{-2} (denoted as Fe_3O_4/RGO-2) was obtained via increasing the amount of $FeCl_2 \cdot 4H_2O$ and $FeCl_3 \cdot 6H_2O$ during synthesis process (Experimental section), and the typical TEM and HRTEM images are shown in Fig. S3. As shown in Fig. 4a, the Fe_3O_4/RGO-2 can deliver capacities of 1834, 1251, 978, 742 and 637 mA h g^{-1} at 0.1, 0.2, 0.5, 1 and 2 A g^{-1}, respectively. The rate capability of Fe_3O_4/RGO-2 from 0.1 to 2 A g^{-1} is about 35%, which is smaller than that of Fe_3O_4/RGO (about 44% from 0.1 to 2 A g^{-1}). This decrease can be attributed to the increased resistance of Fe_3O_4/RGO-2 arising

from the high mass loading of Fe_3O_4, which we will discuss in the following paragraph. As for the capacity did not significantly increase with the increased mass loading of Fe_3O_4, it might be due to the fact that more NPs on the RGO would inevitably pack and aggregate more active NPs, as indicated by HRETM observation (Fig. S3) Nevertheless, the capacities of Fe_3O_4/RGO-2 are still substantially higher than those of the bare Fe_3O_4 NPs. All these results convincingly show that the incorporation of RGO could dramatically improve the capacity and cycling stability of Fe_3O_4.

To gain an in-depth understanding of the enhanced electrochemical performance of Fe_3O_4/RGO composites, electrochemical impedance spectroscopy (EIS) analysis was conducted on bare Fe_3O_4, Fe_3O_4/RGO and Fe_3O_4/RGO-2 electrodes to investigate their electrochemical reaction kinetics. Fig. 4b shows the Nyquist plots of bare Fe_3O_4, Fe_3O_4/RGO and Fe_3O_4/RGO-2 electrodes at fresh coin cells over the frequency range from 100 kHz to 0.01 Hz. All the electrodes present a semicircle in the middle-high frequency region and a sloped straight line in the low frequency region. The semicircle in the moderate high frequency region is assigned to the charge-transfer or electrochemical reaction resistance,[27,29] while the sloped straight at low frequency is related to the diffusion of lithium ions in the active material. Obviously, the charge transfer resistance of Fe_3O_4/RGO and Fe_3O_4/RGO-2 electrode are only 62 and 93 Ω, which are much smaller than that of bare Fe_3O_4 electrode (284 Ω), again confirming the enhanced conductivity of Fe_3O_4/RGO anodes. The larger charge-transfer resistance of Fe_3O_4/RGO-2 than the Fe_3O_4/RGO is due to the increased mass loading of the Fe_3O_4.. Additionally, the relatively more vertical slope also indicates the easier and faster diffusion of lithium ions within the Fe_3O_4/RGO composites electrode.

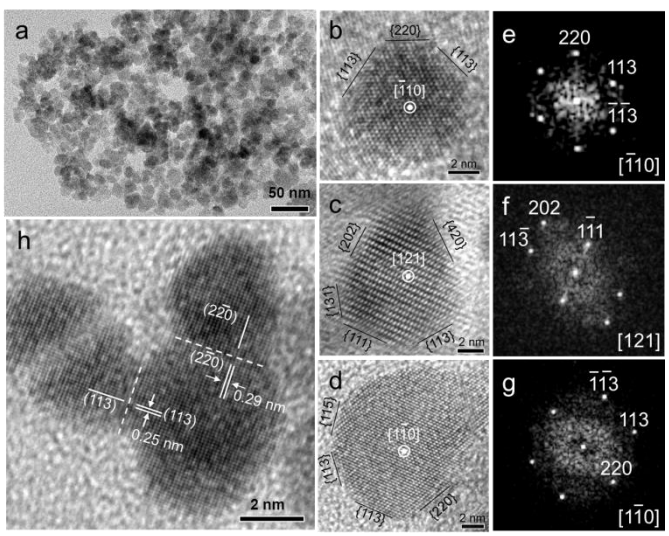

Fig. 5 (a) TEM images of bare Fe_3O_4 nanoparticles. (b, c, d) HRTEM images of individual Fe_3O_4 nanoparticles with irregular shapes. (e, f, g) Fast Fourier Transform (FFT) pattern corresponding to (b), (c) and (d), respectively. (h) HRTEM image of three adjacent Fe_3O_4 NPs viewed along <332>, showing the orientation attachment through coherent interfaces.

HRTEM investigation on the detailed microstructure of the Fe_3O_4 NPs before and after integrating on RGO sheets were also carried out to further understand the origin of the superior electrochemical performances of the Fe_3O_4/RGO composites. Fig. 5a shows the TEM images of typical bare Fe_3O_4 NPs. It can be seen that the as-synthesized Fe_3O_4 NPs existed in the form of irregular polyhedral shapes. HRTEM observation of about 100 randomly selected NPs was performed. Fig. 5b, c and d show some representative HRTEM images of the NPs along different projections. Fourier filtering was used to extract the information of lattice fringes. In order to index the exposed facets, distances and angles of diffractions in the reciprocal space were analyzed. HRTEM studies revealed that these particles are mainly defined by {220} (or equally {110}), {111} and {113} surface facets. In most cases, {113} facets can be frequently observed, while {115} exposed facets can also be seen on the spherical-like particle (as shown in Fig. 5d). In general, high-index surfaces offer a high density of atomic steps, dangling bonds and ledges that act as chemical active sites. [43-46] For magnetite Fe_3O_4 with inverse spinel fcc structure, the {113} and {115} surfaces are composed of low-coordinated surface step atoms (as shown in Fig 6), which can have a strong impact on the surface reactivity. Accordingly, the irregularly shaped Fe_3O_4 NPs are expected to stimulate the reversible conversion reaction by offering abundant surface step atoms that act as electrochemical active sites.[18,47,48] However, NPs with a large portion of surface atoms are both highly active and unstable. In order to reduce the high surface energy, the aggregation of the Fe_3O_4 NPs would be favored,[49,50] especially during the charging and discharging process. More evidences for the aggregation tendency of NPs can be seen from the HRTEM image of three adjacent Fe_3O_4 NPs. As shown in Fig. 5h, distinct interfaces among the particles are observed. It can be seen that the bigger particle is connected with two smaller ones by the {113} and {220} facets, sharing the same crystallographic orientation of <332> zone axis. Obviously, this HRTEM observation confirms that the adjacent Fe_3O_4 NPs in a common crystallographic orientation tend to fuse together by a coherent interface to minimize surface free energies. Therefore, the orientation attachment of the irregularly shaped NPs results in the reduction of surface atoms and electrochemical reactivity sites, which deteriorate the specific capacity and cycle stability, as demonstrated in Fig. 3 and Fig. 4.

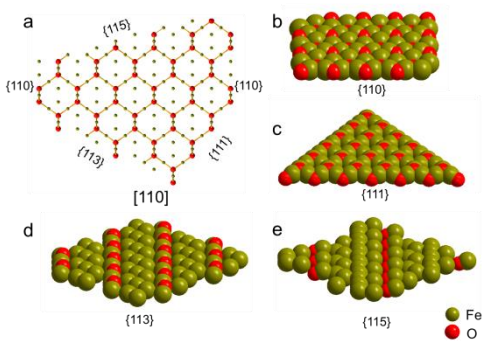

Fig. 6 (a) Atomic ball-stick model of magnetite Fe_3O_4 oriented along [110], in which {110}, {111}, {113} and {115} facets are viewed edge-on. (b-e) Ball models of Fe_3O_4 crystallography planes, showing the atomic arrangements on the {110}, {111}, {113} and {115} facets, respectively. Iron is colored green and oxygen is colored red. The {110} planes are flat with closely packed surface atoms. The {111} planes are composed of zigzag arranged atoms. The {113} and {115} planes are rough with low-coordinated step atoms.

Fig. 7 illustrates the structural features of the Fe_3O_4/RGO composites. Separated Fe_3O_4 NPs with different crystallographic orientation are uniformly dispersed on RGO. Most of the isolated Fe_3O_4 NPs maintain their irregular shapes, suggesting that the step atoms on the high indexed exposed

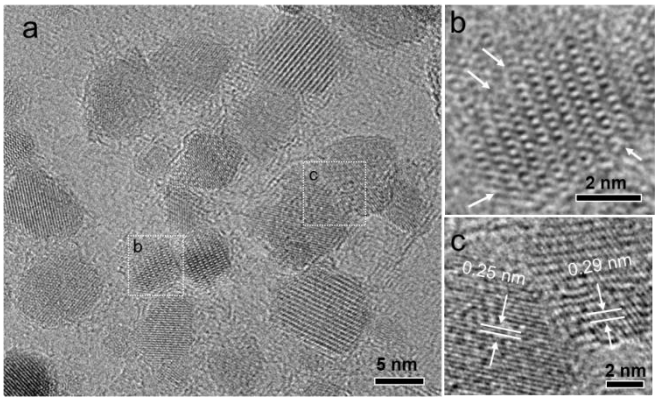

Fig. 7 (a) Typical HRTEM image of Fe_3O_4/RGO composites, showing the uniformly-dispersed Fe_3O_4 nanoparticles deposited on RGO. (b) Magnified HRTEM image of an individual Fe_3O_4 nanoparticle, on which edges and corners can be observed, as indicated by white arrows. (c) HRTEM image of two Fe_3O_4 NPs contacted by incoherent interface.

facets are preserved. As demonstrated in Fig. 7b, edges and corners that benefit the conversion reaction towards lithium storage can be observed on the surface of the isolated particle. Carbon layers attached to the surfaces of isolated particles can also be seen, which indicates that the highly active surfaces could be protected by RGO. The enlarged HRTEM image from square c in Fig. 7 reveals two particles contacted by {220} and {113} facets. The lattice mismatch between {220} and {113} is calculated to be 15.7%, implying that it is difficult for the contacting particles to merge together to form a secondary large particle. According to HRTEM observation of different areas in the copper grid (some typical images are shown in Fig. S4), no oriented attachment of Fe_3O_4 NPs through a coherent interface can be found, suggesting that the interaction between RGO and NPs are so strong that even the contacted NPs cannot rotate and align freely. Based on HRTEM analysis, it is indicated that the RGO is able to hinder the grain rotation and grain realignment that lead to orientation attachment, thus keeping the active materials apart from aggregation. Thereby, the Fe_3O_4 particles deposited on RGO were kept in a small dimension that benefits the electrode performances in two aspects: (1) the volume change during the charging and discharging processes could be accommodated. (2) A large portion of Fe_3O_4 NPs with electrochemical active surfaces maintain contact with the electrolyte, thus allowing readily access of ions and electrons to the active surfaces, which could contribute to the excellent rate performance. At the same time, RGO in the composites provides electron conductive channels among active particles as well as large electrode/electrolyte interfacial contact area as previously reported.[51,52] Hence, combining properties of both high electrochemical activity and high conductivity, RGO sheets loaded by homogeneously dispersed Fe_3O_4 NPs with active surfaces should be responsible for the superior electrochemical performances.

Conclusions

In summary, Fe_3O_4/RGO composites with superior electrochemical performances were successfully prepared by a simple coprecipitation method. The Fe_3O_4/RGO electrode exhibited substantially higher electrochemical performances than bare Fe_3O_4 NPs and RGO electrodes. The Fe_3O_4/RGO composites delivered a high lithium storage capacity and good cycle stability of 1637 mA h g^{-1} at 0.1 A g^{-1} for the 10th cycle and could remain 1397 mA h g^{-1} after 100 cycles. The improved capacities and excellent cycling stability are attributed to the synergistic effect between Fe_3O_4 and RGO, which the Fe_3O_4 NPs provide large portion of electrochemical active sites and the RGO substrate preserves the active surface of Fe_3O_4 and acts as a conducting matrix as well as a volume buffer. These findings provide a new insight into the effect of Fe_3O_4 NPs and RGO on the improvement of electrochemical performances.

Acknowledgements

We acknowledge the support of this work by the Natural Science Foundations of China (21273290 and 91323101), the Natural Science Foundations of Guangdong Province (S2013030013474), the Research Fund for the Doctoral Program of Higher Education of China (20120171110043) and the Young Teacher Starting-up Research of Sun Yat-Sen University.

Notes and references

[a] *KLGHEI of Environment and Energy Chemistry, MOE of the Key Laboratory of Bioinorganic and Synthetic Chemistry, School of Chemistry and Chemical Engineering, Sun Yat-Sen University, Guangzhou 510275, People's Republic of China. E-mail: chedhx@mail.sysu.edu.cn; luxh6@mail.sysu.edu.cn; Fax: +86-20-84112245; Tel: +86-20-84110071*

[b] *Instrumental Analysis and Research Centre, Sun Yat-Sen University, Guangzhou 510275, People's Republic of China.*

Electronic Supplementary Information (ESI) available. See DOI: 10.1039/b000000x/

1. M. Armand and J. M. Tarascon, *Nature*, 2008, **451**, 652-657.
2. W. M. Zhang, X. L. Wu, J. S. Hu, Y. G. Guo and L. J. Wan, *Adv. Funct. Mater.*, 2008, **18**, 3941-3946.
3. B. Scrosati and J. Garche, *J. Power Sources*, 2010, **195**, 2419-2430.
4. G. L. Xu, Y. F. Xu, J. C. Fang, F. Fu, H. Sun, L. Huang, S. Yang and S. G. Sun, *ACS Appl. Mater. Inter.*, 2013, **5**, 6316-6323.
5. Y. Xie and C. Wu, *Dalton T.*, 2007, 5235-5240.
6. J. Jiang, Y. Li, J. Liu, X. Huang, C. Yuan and X. W. Lou, *Adv. Mater.*, 2012, **24**, 5166-5180.
7. Y. Liu and X. Zhang, *Electrochim. Acta*, 2009, **54**, 4180-4185.
8. S. Mitra, P. Poizot, A. Finke and J. M. Tarascon, *Adv. Funct. Mater.*, 2006, **16**, 2281-2287.
9. W. Chen, S. Li, C. Chen and L. Yan, *Adv. Mater.*, 2011, **23**, 5679-5683.
10. L. Wang, H. Ji, S. Wang, L. Kong and G. Yang, *Nanoscale*, 2013, **5**, 3793-3799.
11. R. Li, X. Ren, F. Zhang, C. Du and J. Liu, *Chem. Commun.*, 2012, **48**, 5010-5012.
12. P. L. Taberna, S. Mitra, P. Poizot, P. Simon and J. M. Tarascon, *Nat. Mater.*, 2006, **5**, 567-573.
13. C. Yang, J. Wu and Y. Hou, *Chem. Commun.*, 2011, **47**, 5130-5141.
14. Q. Q. Xiong, Y. Lu, X. L. Wang, C. D. Gu, Y. Q. Qiao and J. P. Tu, *J. Alloy. Comp.*, 2012, **536**, 219-225.
15. J. Hou, Y. Shao, M. W. Ellis, R. B. Moore and B. Yi, *Phys. Chem. Chem. Phys.*, 2011, **13**, 15384-15402.

16. J. Xiao, G. Xu, S. G. Sun and S. Yang, *Part. Part. Syst. Char.*, 2013, **30**, 893-904.
17. C. Ban, Z. Wu, D. T. Gillaspie, L. Chen, Y. Yan, J. L. Blackburn and A. C. Dillon, *Adv. Mater.*, 2010, **22**, E145-E149.
18. Z. M. Cui, L. Y. Jiang, W. G. Song and Y. G. Guo, *Chem. Mater.*, 2009, **21**, 1162-1166.
19. J. Z. Wang, C. Zhong, D. Wexler, N. H. Idris, Z. X. Wang, L. Q. Chen and H. K. Liu, *Chem–Eur. J.*, 2011, **17**, 661-667.
20. L. Wang, Y. Yu, P. C. Chen, D. W. Zhang and C. H. Chen, *J. Power Sources*, 2008, **183**, 717-723.
21. X. Lu, H. Dou, B. Gao, C. Yuan, S. Yang, L. Hao, L. Shen and X. Zhang, *Electrochim. Acta*, 2011, **56**, 5115-5121.
22. K. S. Novoselov, A. K. Geim, S. V. Morozov, D. Jiang, Y. Zhang, S. V. Dubonos, I. V. Grigorieva and A. A. Firsov, *Science*, 2004, **306**, 666-669.
23. M. J. Allen, V. C. Tung and R. B. Kaner, *Chem. Rev.*, 2009, **110**, 132-145.
24. P. Lian, X. Zhu, H. Xiang, Z. Li, W. Yang and H. Wang, *Electrochim. Acta*, 2010, **56**, 834-840.
25. L. Ji, Z. Tan, T. R. Kuykendall, S. Aloni, S. Xun, E. Lin, V. Battaglia and Y. Zhang, *Phys. Chem. Chem. Phys.*, 2011, **13**, 7170-7177.
26. J. Su, M. Cao, L. Ren and C. Hu, *J. Phys. Chem. C*, 2011, **115**, 14469-14477.
27. R. Wang, C. Xu, J. Sun, L. Gao and C. Lin, *J. Mater. Chem. A*, 2013, **1**, 1794-1800.
28. S. H. Lee, S. H. Yu, J. E. Lee, A. Jin, D. J. Lee, N. Lee, H. Jo, K. Shin, T. Y. Ahn, Y. W. Kim, H. Choe, Y. E. Sung and T. Hyeon, *Nano Lett.*, 2013, **13**, 4249-4256.
29. Y. Chang, J. Li, B. Wang, H. Luo, H. He, Q. Song and L. Zhi, *J. Mater. Chem. A*, 2013, **1**, 14658-14665.
30. Y. Wu, Y. Wei, J. Wang, K. Jiang and S. Fan, *Nano Lett.*, 2013, **13**, 818-823.
31. X. Y. Peng, X. X. Liu, D. Diamond and K. T. Lau, *Carbon*, 2011, **49**, 3488-3496.
32. W. S. Hummers and R. E. Offeman, *J. Am. Chem. Soc.*, 1958, **80**, 1339-1339.
33. Z. Wang, X. Zhou, J. Zhang, F. Boey and H. Zhang, *J. Phys. Chem. C*, 2009, **113**, 14071-14075.
34. O. N. Shebanova and P. Lazor, *J. Solid State Chem.*, 2003, **174**, 424-430.
35. P. R. Graves, C. Johnston and J. J. Campaniello, *Mater. Res. Bull.*, 1988, **23**, 1651-1660.
36. V. Chandra, J. Park, Y. Chun, J. W. Lee, I. C. Hwang and K. S. Kim, *ACS Nano*, 2010, **4**, 3979-3986.
37. D. Zhang, Z. Liu, S. Han, C. Li, B. Lei, M. P. Stewart, J. M. Tour and C. Zhou, *Nano Lett.*, 2004, **4**, 2151-2155.
38. T. Fujii, F. M. F. de Groot, G. A. Sawatzky, F. C. Voogt, T. Hibma and K. Okada, *Phys. Rev. B*, 1999, **59**, 3195-3202.
39. F. He, J. Fan, D. Ma, L. Zhang, C. Leung and H. L. Chan, *Carbon*, 2010, **48**, 3139-3144.
40. L. Wang, J. Liang, Y. Zhu, T. Mei, X. Zhang, Q. Yang and Y. Qian, *Nanoscale*, 2013, **5**, 3627-3631.
41. B. Jang, M. Park, O. B. Chae, S. Park, Y. Kim, S. M. Oh, Y. Piao and T. Hyeon, *J. Am. Chem. Soc.*, 2012, **134**, 15010-15015.
42. C. He, S. Wu, N. Zhao, C. Shi, E. Liu and J. Li, *ACS Nano*, 2013, **7**, 4459-4469.
43. J. Yin, Z. Yu, F. Gao, J. Wang, H. Pang and Q. Lu, *Angew. Chem. Int. Edit.*, 2010, **49**, 6328-6332.
44. H. B. Jiang, Q. Cuan, C. Z. Wen, J. Xing, D. Wu, X. Q. Gong, C. Li and H. G. Yang, *Angew. Chem. Int. Edit.*, 2011, **50**, 3764-3768.
45. Y. Sun and Y. Xia, *Science*, 2002, **298**, 2176-2179.
46. N. Tian, Z. Y. Zhou, S. G. Sun, Y. Ding and Z. L. Wang, *Science*, 2007, **316**, 732-735.
47. P. Poizot, S. Laruelle, S. Grugeon, L. Dupont and J. M. Tarascon, *Nature*, 2000, **407**, 496-499.
48. J. Jamnik and J. Maier, *Phys. Chem. Chem. Phys.*, 2003, **5**, 5215-5220.
49. J. W. Lee, T. Ahn, J. H. Kim, J. M. Ko and J. D. Kim, *Electrochim. Acta*, 2011, **56**, 4849-4857.
50. B. Jia and L. Gao, *J. Phys. Chem. C*, 2007, **112**, 666-671.
51. H. Wang, L. F. Cui, Y. Yang, H. Sanchez Casalongue, J. T. Robinson, Y. Liang, Y. Cui and H. Dai, *J. Am. Chem. Soc.*, 2010, **132**, 13978-13980.
52. H. Zhang, X. Yu, D. Guo, B. Qu, M. Zhang, Q. Li and T. Wang, *ACS Appl. Mater. Inter.*, 2013, **5**, 7335–7340.